

Surface subsidence induced by the Crandall Canyon Mine (Utah) collapse: InSAR observations and elasto-plastic modelling

Q1

C. Plattner,^{1,2} S. Wdowinski,¹ T. H. Dixon¹ and J. Biggs^{1*}

¹Rosenstiel School of Marine and Atmospheric Sciences, Marine Geology and Geophysics, University of Miami, 4600 Rickenbacker Causeway, Miami, FL 33149, USA. E-mail: cplattner@rsmas.miami.edu

²Dept. of Earth and Environmental Sciences, former at Ludwigs-Maximilians-Universitaet, Theresienstr. 41, 81377 Muenchen, Germany

Accepted 2010 September 3. Received 2010 September 2; in original form 2010 April 22

SUMMARY

The Crandall Canyon Mine, Utah, collapse in August 2007 resulted in a total of nine fatalities. We processed data from the ALOS satellite acquired before and after the collapse to quantify surface subsidence associated with the collapse to better understand the collapse process. The deformation shows a steep V-shaped pattern of subsidence with slight asymmetry. We compare the fit of four different models that simulate the subsidence pattern. The first two models use elastic half-space rheology. We find that collapse alone cannot explain the observations, and a component of normal faulting is required to fit the data. The second set of models simulates collapse in elasto-plastic media. Only a small component of normal faulting is required in these models. We suggest that considering elasto-plastic material behaviour is particularly important for shallow deformation modelling, where microfractures and other non-elastic rheology are common. Disregarding this material behaviour can lead to biased model parameter estimates.

Key words: Geomechanics; Elasticity and anelasticity; Dynamics and mechanics of faulting; Mechanics; theory and modelling; Rheology: crust and lithosphere.

1 INTRODUCTION

On 2007 August 6, the Crandall Canyon coalmine in central Utah underwent a tragic collapse, killing six miners. Ten days later, on August 16, a second collapse occurred, killing three rescuers and injuring several others. The mine exploited a 2.4 m thick seam of bituminous coal in Cretaceous elastic sedimentary rocks at a depth of about 600 m. The mine was an underground ‘room and pillar’ type, whereby pillars of coal are left to support the overlying strata during mining. At the time of the collapse, pillar ‘recovery’ (removal or reduction of pillars) was being practiced (Gates *et al.* 2007).

The seismic event of 2007 August 6, shows a dominantly implosional source mechanism, consistent with the collapse of an underground cavity (Dreger *et al.* 2008; Ford *et al.* 2008). Seismological modelling based on the known mine depth of 600 m and calculations of coal volume expansion into the voids between the mine pillars constrain the maximum allowable roof-floor closure (0.3 m–0.5 m) and suggest a horizontal collapse area of about 920 × 220 m² elongated in the east–west direction (Pechmann *et al.* 2008). However, a closing horizontal crack would not be expected to generate Love Waves and a secondary source is required to fit the observations, which accounts for a further 24 per cent of the collapse-related moment (Dreger *et al.* 2008, Ford *et al.* 2008).

*Now at: COMET, Department of Earth Sciences, University of Oxford, Parks Road, Oxford, OX1 3PR, UK.

The moment tensor decomposition is non-unique, but is consistent with slip on a steeply dipping normal fault which may have been stimulated by stress changes associated with the cavity collapse (Pechmann *et al.* 2008). No evidence for surface rupture has been found in the Crandall Canyon mine area (Gates *et al.* 2007).

Previous studies have used using Satellite Aperture Radar Interferometry (InSAR) to monitor and interpret surface subsidence from underground excavations and collapse in active mining regions (Carnec *et al.* 1996; Massonnet & Feigl 1998; Ge *et al.* 2007; Ng *et al.* 2009). We apply InSAR to observe the surface subsidence above the Crandall Canyon Mine associated with one or both collapses (August 6, 16) and accompanying seismicity. In this paper, we describe the InSAR results and develop and compare several models for the surface subsidence at Crandall Canyon Mine, with the goal of obtaining insight into the rheological behaviour of near-surface materials. In particular, we present a new analytical model that accounts for subsidence above an elliptical cavity in elasto-plastic media and considers an overlying subsiding wedge, the boundaries of which limit the lateral extent of the subsidence trough.

2 SURFACE DEFORMATION ANALYSIS

2.1 Insar analysis

InSAR is a satellite-based geodetic technique, which calculates a dense grid (~30 m pixel resolution) of surface deformation by

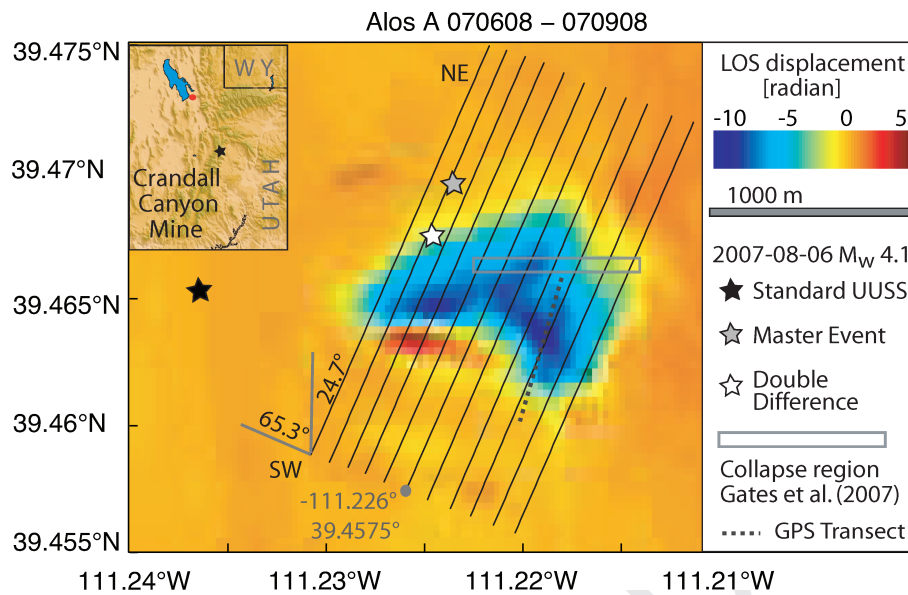


Figure 1. ALOS Interferogram showing LOS displacement in radians (1 radian = 11.8 cm). 11 profiles (black lines) spanning the deformation region capture the gradient of deformation from southwest to northeast (24.7° cw from north) and are used to calculate the mean 2-D deformation (Fig. 2). The plot also shows the three different epicentre locations for the 2007 August 6 seismic event and the estimated collapse region (rectangle) from Pechmann *et al.* (2008).

measuring the phase difference in each pixel between successive radar images (Bürgmann *et al.* 2000). We use data from the Japanese L-band satellite ALOS, which transmits a radar signal with a wavelength of 23.6 cm. Our study is based on two images acquired on 2007 June 8 and 2007 September 8, giving a 3 month temporal baseline and a 637 m perpendicular geometrical baseline. We processed the data using the JPL software ROI_PAC to generate an interferogram spanning the event and use an oversampled SRTM DEM to correct for topographic effects. The interferogram has an excellent coherence across the entire image (Fig. 1), despite the construction of new roads and pads, which graded into the hill slope for the emergency drilling operations. These drill pads and roads significantly altered the ground surface, but only along linear features and, hence, had a limited impact on the interferometric coherence.

The deformation pattern is elliptically shaped and spans about 1500 m in the northwest–southeast direction and 1000 m in the orthogonal northeast–southwest direction (Fig. 1). The major part of the deforming region shows increasing line-of-sight (LOS) displacement of ~ 10 radians (equivalent to about 18 cm). Using a single interferogram, it is not possible to distinguish between horizontal and vertical deformation. For simplicity here, we assume that the entire motion is vertical (implications of this assumption are discussed in the model results) and translate the observed phase change U_{LOS} to vertical surface displacement U_z by:

$$U_z = \frac{U_{LOS}}{\cos(34.3^\circ)}. \quad (1)$$

The maximum subsidence is therefore 27.4 cm. The subsidence pattern shows an asymmetry in the southwest–northeast direction, with a narrow region of uplift along the southwestern rim.

2.2 Constraints on timing of subsidence

Between 2000 and 2007 campaign GPS measurements were conducted along a transect spanning the Crandall mine region (Fig. 1). Between the occupations in 2004 and 2007 August (spanning both

collapse events), these data show 30 cm of subsidence in the northern part of this transect (unfortunately, measurements in the south are not available; Gates *et al.* 2007). No subsidence was detected in interferograms between 2006 December and 2007 June (Gates *et al.* 2007), but nearly the full 30 cm is recorded for the period 2007 June–September. We conclude that the great majority of the observed subsidence is associated with the collapse events between August 6 and August 16 and note that the maximum GPS-recorded subsidence is similar to the InSAR observed subsidence under the assumption that most of the LOS change is in the vertical component.

2.3 2-D displacement profiles

To characterize the deformation pattern, we use a series of profiles in the southwest–northeast direction (Fig. 1). This direction (24.7° clockwise from north) was chosen perpendicular to the elongated feature along the southwest rim that exhibits positive LOS displacement. It is also approximately perpendicular to the strike of the double-couple moment tensor solution (149° clockwise from north; Ford *et al.* 2008). Each profile covers 62 pixels of the InSAR image (~ 2 km). The vertical displacement from each profile is shown in Fig. 2 as grey solid lines, while the mean displacement profile is the thick black solid line. This mean-displacement profile is V-shaped with a slight asymmetry, as the southwestern slope is steeper and shows some uplift with respect to the less steep northeastern slope where no significant uplift is found. The V-shape subsidence pattern is expected for an underground collapse, while the asymmetry could be interpreted to result from normal faulting.

We also plotted the elevation along the displacement profiles (Fig. 2) to evaluate possible topographic effect on half-space deformation models, because neglecting topography in such models can introduce biases (Cayol & Cornet 1998; William & Wadge 2000). Our elevation profile analysis shows that the differential elevation in the individual profiles is in the range of 100–300 m and the mean differential elevation ~ 175 m. Topographic effects on the models are discussed below.

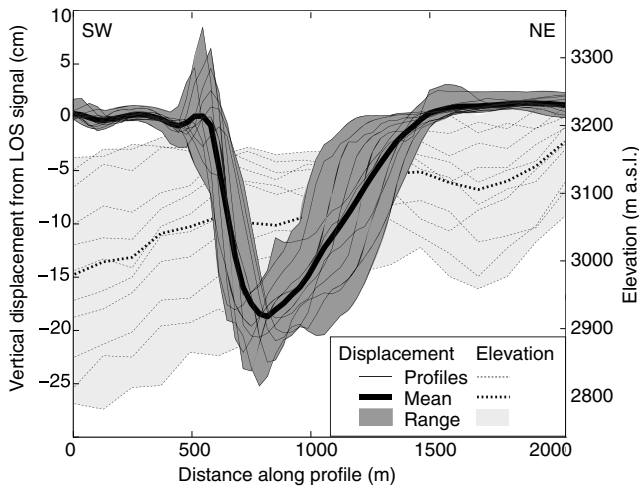


Figure 2. 2-D surface displacement and topography profiles across the study area. Thin solid lines show vertical displacement computed from InSAR line of sight displacement (eq. 1) and thin dotted lines show elevation along southwest–northeast profiles (Fig. 1). The thick solid and dotted black lines mark the mean displacement and elevation, respectively, the shaded areas mark the range of values. Ratio of vertical to horizontal scale is 2 : 1. Given a source depth of 600 m, the elevation of the collapse area is approximately 2600 m a.s.l.

3 DEFORMATION MODELLING

In the following, we explore different models that can explain the overall subsidence pattern and magnitude and compare them to the observations. We use a grid search to find the best-fitting parameters for each model, using the Root Mean Square (rms) misfit to the profile to assess quality of fit. We consider only model solutions that match the maximum subsidence amplitude to within the standard deviation of the mean deformation as computed from the eleven displacement profiles ($-18.6 \text{ cm} \pm 2.4 \text{ cm}$).

3.1 Elastic dislocation model

Our analytical modelling is first performed using the Okada formulation for motion on a rectangular dislocation within a homogenous, isotropic elastic half-space (Okada 1985). Initially, we estimate the subsidence from underground collapse alone and then consider a combination of underground collapse and normal faulting.

3.1.1 Subsidence from collapse only

We model underground collapse (sudden roof–floor-closure) by a horizontal tensional dislocation with a negative displacement (often referred to as an antisill) striking parallel to the 2-D displacement profile (Fig. 3a). We fix the source depth to 600 m. The free model parameters are the width of the antisill w (with $w \leq 1000 \text{ m}$, assuming it to be smaller than the observed collapse width) and the imposed tensional dislocation d (with $d \geq -0.5 \text{ m}$). Initially, we calculate a 3-D model to obtain the best estimate of the dislocation d and a realistic geodetic moment. In this model, we constrain the collapse length l to be equal to the collapse width w . We also calculate a 2-D solution (simulating the plane strain assumption by using a sufficiently long collapse length l) for subsequent comparison to a plain strain elasto-plastic model. Fig. 4 illustrates the trade-off between length and width for the 3-D model ($l = \infty$ is equivalent

to the 2-D model). Results for the 3-D and 2-D models are shown in Fig. 3(b).

The best-fitting 3-D model solution (Fig. 3b) shows a broad surface subsidence trough with rms of 4.1 cm, somewhat larger than the standard deviation of the displacement profiles shown in Fig. 1 (2.4 cm). The mine depth is well constrained and variations within reasonable limits (down to 400 m) cannot explain this misfit (if we solve for source depth we obtain an anomalously shallow result of 200 m). Our best-fit model uses the largest possible displacement d (-0.5 m). Allowing for $d \geq -2.4 \text{ m}$ (coal seam height) does not provide an acceptable misfit (defined by rms $< 2.4 \text{ cm}$). Thus, also asymmetric collapse cannot explain the data. The horizontal collapse area ($w \times l$) needed to fit the data is $\sim 0.36 \text{ km}^2$ and varies only slightly (-10 per cent) for other plausible geometries (Fig. 4). We calculate the vertical component of the moment tensor (in Nm):

$$M_0 = M_{zz} = -(\lambda + 2\mu) S d, \quad (2)$$

where λ is the Lamé modulus (1×10^{10}) and μ is the shear modulus (9.25×10^9) (Ford *et al.* 2008) and S is the collapse area ($w \times l$). The geodetic moment for the collapse is calculated using the formula from Hanks & Kanamori (1979)

$$M_w = \frac{2}{3} \log M_0 - 10.7, \quad (3)$$

where M_0 has been converted from Nm^{-1} ($M_0 = 5.13 \times 10^{15} \text{ Nm}^{-1}$) into dyne cm^{-1} . We obtain $M_w = 4.4$, which is larger than the published seismic moment ($M_w = 4.1$). This discrepancy can be explained by subsequent deformation, such as the collapse at 2007 August 16th, being recorded in the InSAR data and not reflected in the seismic solution. The plane strain solution does not differ in shape from the 3-D solution (Fig. 3b). The collapse width in the plane strain model (325 m) does not significantly differ from the collapse width in a model where the collapse length has a large, but plausible extent (e.g. $l = 1000 \text{ m}$; Fig. 4). Therefore we find that using the plane strain geometry is acceptable.

We tested the influence of topography by superimposing the surface deformation signals of incremental collapse sources with their depths increasing linearly from 600 to 425 m (mean differential topography is 175 m). We keep the total width w of 325 m and displacement $d = 0.5 \text{ m}$ equal to that in our 2-D best-fit solution. The results indicate that the topographic effect cannot explain the model misfit. For the maximum differential topography (300 m) we find that the shallower source depth in the southwest increases the surface subsidence and could partially explain the steeper slope at the southwest rim (Fig. 5a).

In Fig. 5(b), we show that the horizontal displacement in our 2-D best-fit model is about six times smaller than the vertical displacement. Since InSAR is more sensitive to the vertical component of the signal, we find that modelling only the vertical component is justifiable.

3.1.2 Subsidence from collapse and normal faulting

To better explain the deformation asymmetry we add a dip-slip displacement along an inclined fault (normal fault) to this model (Fig. 3c). Such faults may form in response to high stresses associated with cavity collapse, especially at the edges of the collapse zone (McGarr *et al.* 1975). We assume that the fault strikes perpendicular to the 2-D displacement profiles (114.7° cw from north) and extends from the mine depth of -600 m towards the surface, simulating the propagation of brittle failure upward from the mine roof. We use the 3-D Okada-based calculations and solve for normal

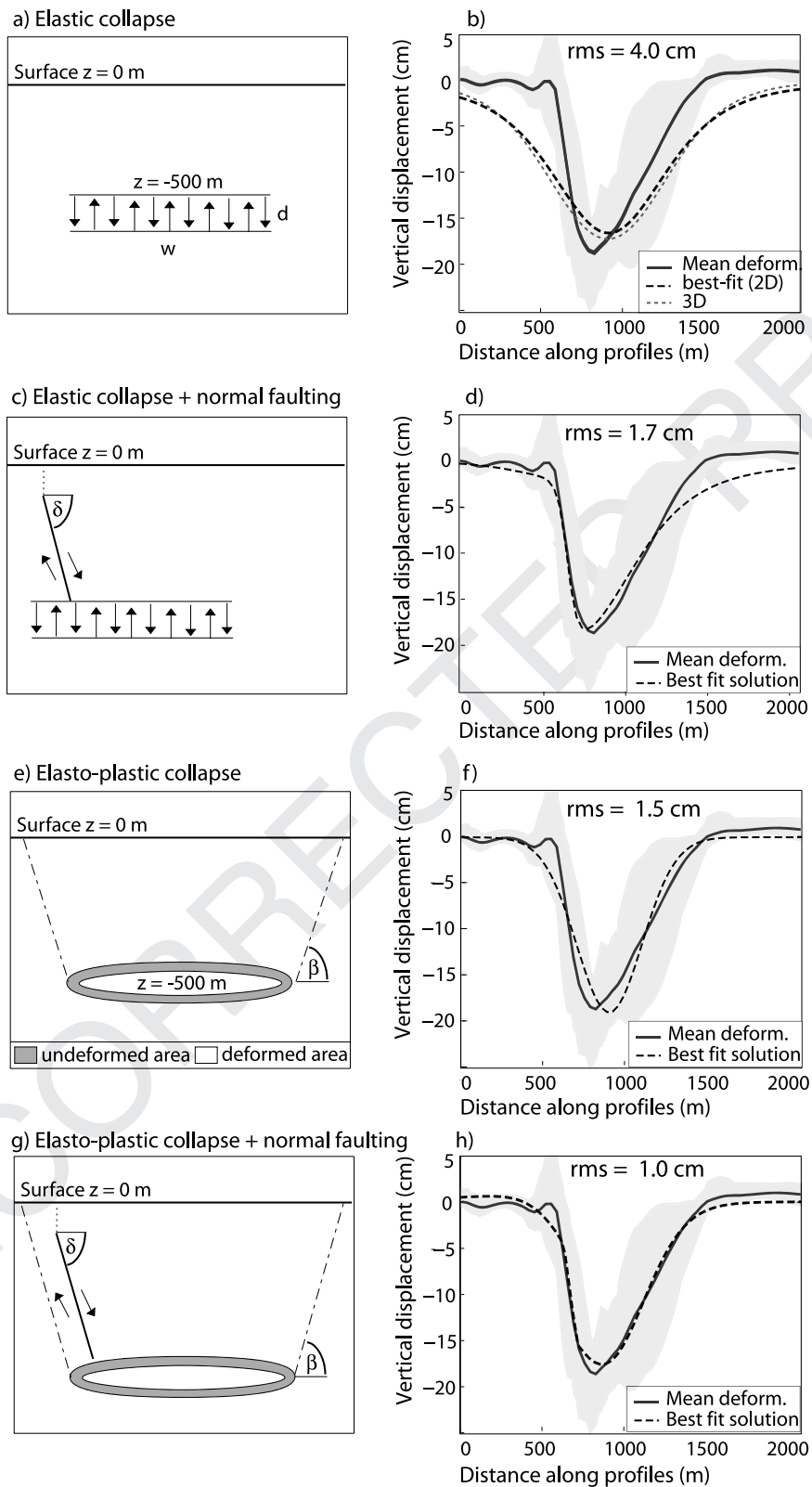


Figure 3. Sketches of model deformation source mechanisms (left panel) and corresponding best fit model (Table 1) and data (right panel): (a) The elastic collapse model has a horizontally aligned negative tensional dislocation as the source geometry. (b) This model fails to explain the narrow subsidence trough. (c) Model combining the elastic collapse with a steep dipping normal fault that originates at the depth of the mine. (d) Normal faulting narrows the subsidence trough and can explain the subsidence asymmetry. (e) The elasto-plastic collapse model simulates subsurface collapse as the volume (area) loss of an ellipse (area loss = undeformed area–deformed area), where wedge boundaries limit the lateral extent of the surface subsidence trough (Fig. 4). (f) The elasto-plastic collapse model explains localization of subsidence well, but fails to explain the subsidence asymmetry. (g) Combination of the elasto-plastic model and a normal fault (in elastic media). (h) This model provides the best fit to the surface observations.

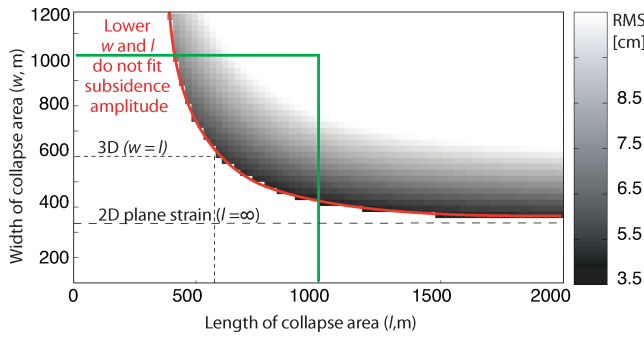


Figure 4. Solution misfits for models assuming only cavity collapse in an elastic half-space show trade-offs between collapse length l and collapse width w . Displacement d is assumed to be -0.5 m (Fig. 4a). Collapse area ($w \times l$) is approximately 0.3 km^2 for all models within the area marked by the green lines. The exact collapse area and the best-fit collapse width w depend on the assumed collapse length l . In the plane strain geometry model (l approaching infinity) only small w (325 m) is required (thick dashed line). Deviations from plane strain geometry (with l becoming progressively smaller) require larger collapse width w (indicated by the red curve). Assuming $w = l$ the collapse area is 600×600 m (thin dashed line). The range of possible solutions for l and w is limited, as the collapse dimension cannot be longer than the observed subsidence trough length (approximately 1000 m, marked by the green line for l and w).

faulting and collapse simultaneously. Our free model parameters are the normal fault width (extent below the surface) se , fault dip δ , dip-slip displacement d_2 and the collapse displacement d (the collapse width is fixed to 325 m since the model cannot resolve the trade-off between d and w within our parameter range). We also solve for the horizontal position of both deformation sources.

Our best-fit solution provides a good fit to the data (rms = 1.7 cm). The contribution of normal faulting narrows the subsidence region and steepens the boundary, in particular to the southwest (Fig. 3d). The two-source model therefore explains the observed deformation asymmetry quite well. Solutions that best satisfy the data (Table 1) have a fault surface that extends close to, but does not reach the surface ($se = -80$ m) in agreement with the observation that no surface rupture was found in the Crandall mine area. The fault dip is not well constrained, but we can exclude dip angles not compatible with a geometry where normal faulting was triggered

by the mine collapse ($\delta > 90^\circ$). The best-fit fault slip depends on the fault dip angle and we exclude solutions where the amount of faulting disagrees significantly with the seismological data, that is, accounts for more than ~ 30 per cent of the collapse moment (here dip angles $< 75^\circ$). We calculate the moment from faulting

$$M_0 = \mu S d_2 \quad (4)$$

and compare the result to the moment from the collapse (eq. 2). In both equations we assume the deformation source length l to be 1000 m, an acceptable value that does not differ significantly from plane strain geometry (Fig. 4). In our best-fit model, the geodetic moment from normal faulting is 29 per cent of the geodetic moment from collapse (Table 1; seismological data suggest 24 per cent).

3.2 Elasto-plastic collapse modelling

The model described above considers deformation in an elastic medium but at this shallow depth purely elastic behaviour is unlikely. We now investigate whether the observed deformation can also be described with a single source of collapse of a non-spherical cavity in an elasto-plastic medium. We adopt the 2-D model of Loganathan & Poulos (1998), which describes subsurface deformation and surface subsidence from excavation of tunnels in clay soils (Figs 3e and 6). We modify the model source geometry from a circle to an ellipse described by its major axis Ra and minor axis Rb , to better account for the elongate shape of the collapsed mine. We obtain the following equation for surface displacement U_z :

$$U_z = \varepsilon R a R b \left[\frac{4H(1-\nu)}{H^2 + x^2} \right] \exp \left(- \left[\frac{1.38x^2}{(H \cot \beta + Ra)^2} \right] \right), \quad (5)$$

where H is the mine centre depth, x is the horizontal distance to the source centre, ν is the Poisson ratio and ε is the strain. The vertical collapse area Ac (comparable to $w \times d$ in the elastic model, striking parallel to the 2-D displacement profiles) can therefore be calculated as

$$Ac = \pi R a R b \varepsilon. \quad (6)$$

The elasto-plasticity parameter β is the dip angle of the collapse wedge boundary shown in Figs 3(c) and 5. Following Loganathan

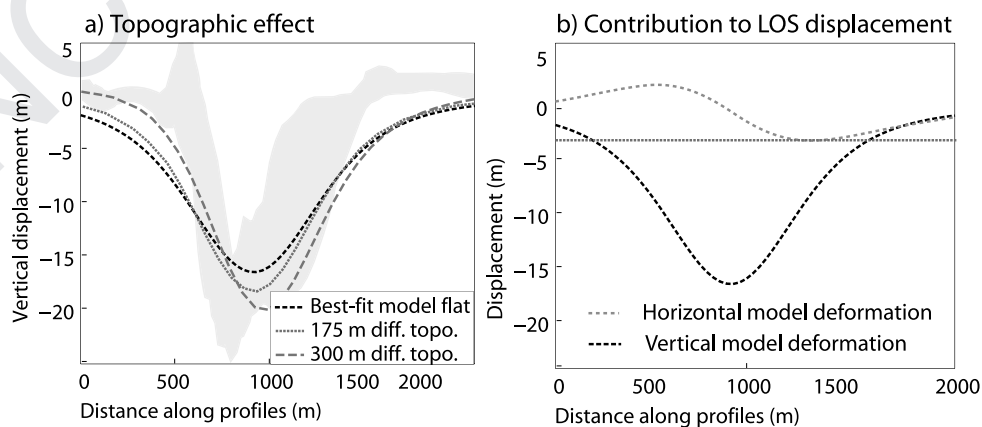


Figure 5. Influence of some model assumptions on best-fit solution of elastic collapse model (Table 1). (a) Non-uniform cavity closure with displacement d ranging from -2.4 to -0.5 m (here linear decrease) can only partially explain the asymmetry, but do not reduce the misfit in the north-east. (b) Topographic effects are simulated by a differential source depth of 300 m (300 m–600 m), but can only partially explain the asymmetry and do not reduce the misfit in the north-east. (c) The contribution of the horizontal deformation signal to the LOS signal is small in comparison to the vertical deformation signal. The total LOS signal is mainly influenced by a lateral shift when neglecting the horizontal component of the subsidence signal.

Table 1. Best-fit model parameters.

Modeltype	Best-fit solution parameters	Range of parameters with acceptable fits (rms < 2.4 cm ^a)	rms (cm)	N ^b	M0 [Nm] Mw ^c
Collapse in elastic medium (2-D)	$w = 325$ m $d = -0.50$ m $X = 925$ m $LL = -111.2304$; 39.4673	–	4.0	3	4.6×10^{15} 4.4
Collapse in elastic medium (3-D)	$w = l = 600$ m $d = -0.50$ m $X = 900$ m $LL = -111.2304$; 39.4671	–	4.1	3	5.13×10^{15} 4.4
Collapse and normal faulting in elastic medium (2-D) ^d	$w = 325$ m $d = -0.35$ m $X = 800$ m $LL = -111.2305$; 39.4662 $d2 = 0.20$ m $\delta = 85^\circ$ $se = -80$ m ($w = 422$ m) $X = 650$ m at $z = 260$ m $LL = -111.2306$; 39.4648	$d = -0.3-0.35$ m $X = 750-875$ m $d2 = 0.15-0.2$ m $\delta = 75^\circ-90^\circ$ $se = -100-20$ m $X = 575-700$ m	1.7	6	3.2×10^{15} 4.3 9.6×10^{14} 4.0
Collapse in elasto-plastic medium (2-D)	$Ra = 225$ m ($\cong w = 450$ m) $\varepsilon = 0.14$ ($\cong d = 2 \times Rb \times \varepsilon = 0.34$ m) $X = 900$ $LL = -111.2304$; 39.4671	$Ra = 125 - 325$ m ($\cong w = 250 - 650$ m) $\varepsilon = 0.1-0.21$ ($\cong d = 0.24-0.5$ m) $X = 850 - 950$	1.5	3	3.4×10^{15} 4.3
Collapse in elasto-plastic medium and normal faulting in elastic medium (2-D) ^e	$Ra = 150$ m ($\cong w = 300$ m) $\varepsilon = 0.15$ ($d = 2 \times Rb \times \varepsilon = 0.28$ m) $X = 825$ $LL = -111.2304$; 39.4664 $d2 = 0.1$ m $\delta = 60^\circ$ $se = 20$ m $X = 625$ at $z = 290$ m $LL = -111.2306$; 39.4646	$Ra = 100 - 250$ m $\varepsilon = 0.09-0.21$ $X = 725 - 975$ $d2 = 0.05-0.15$ m $\delta = 50^\circ - 90^\circ$ $se = -100-0$ m $X = 550 - 775$	1.0	7	2.6×10^{15} 4.2 6.3×10^{14} 3.8

Notes: In all models the collapse source strikes parallel (24.7° cw from north) and the normal fault perpendicular ($\sim 114.7^\circ$ cw from north) to the 2-D displacement profiles. w , fault width (m); l , fault length (m) (in 3-D model, in 2-D fixed); d , displacement on antisill (m); X , fault centre location as distance (m) along profiles (Fig. 2); LL , longitude and latitude of X along the centre profile (Fig. 1); z , depth of X (for horizontal collapse sources fixed to 600 m); se , fault end below surface (m); $d2$, slip on normal fault (m); δ , fault dip angle; Ra , ellipse major axis (m); $e0$, strain.

^a2.4 cm represents the standard deviation of the profiles from the mean surface deformation (Fig. 2).

^bNumber of free variables in the model.

^cM0 is the scalar moment, Mw the moment magnitude as computed from eqs (2) and (3), in plane strain geometry (2-D) with $l = 1000$ m (Fig. 4).

^d w is fixed, acceptable solutions have a moment from faulting that is less than 35 per cent of the collapse moment.

^eThe elasto-plastic collapse model provides acceptable fits to the data without faulting. To constrain sensitivity to the fault parameters we set the minimum slip to 0.05 m, se to shallower than 100 m and the range of solutions to a fit better than rms = 1.5 (rms of the best-fitting elasto-plastic model without faulting).

& Poulos (1998) we assume $\beta = 45^\circ$ (assuming weak material), where β is related to the material friction angle ϕ by

$$\beta = 45 + \frac{\phi}{2}. \quad (7)$$

As before, we fix the cavity centre depth H at the mine depth of 600 m and set Poisson ratio ν to 0.25. We fix Rb to 1.2 m, which is equivalent to half the minimum cavity height (here, the height of the coal seam). We solve for the free model parameters Ra (with

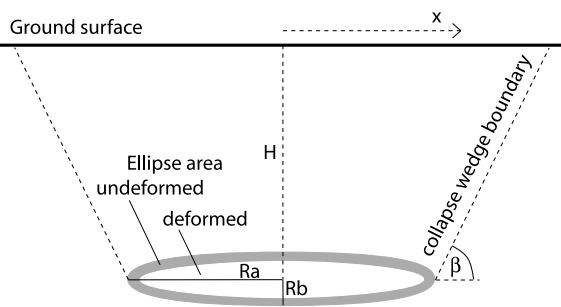


Figure 6. Schematic illustration of the elasto-plastic collapse model, modified from Loganathan & Poulos (1998). The elliptical source geometry is defined by its major axis Ra in x -direction and minor axis Rb in z -direction. The lateral extent of the subsidence trough is controlled by angle of the wedge boundaries from horizontal (β). The area loss of the cavity cross-section is defined by strain ε (see eq. 6).

$Ra \leq 500$ m, equivalent to half the collapse width w in the elastic model) and ε , constraining the maximum subsidence amplitude to the standard deviation of the mean deformation. As in the elastic collapse model, we assume again that the vertical closure is less than 0.5 m (as $Ra \gg Rb$ we assume only changes in Rb , with 0.5 m being equivalent to $\varepsilon < 0.21$).

The model solution predicts a narrow subsidence trough and provides a good fit to the mean displacement profile (rms = 1.5 cm; Fig. 3f). The best-fitting model parameters (Table 1) provide plausible values for the source geometry ($Ra = 225$ m, thus the collapse width is 450 m and $\varepsilon = 0.15$, so that the vertical closure $2 \times Rb \times \varepsilon = 0.4$ m). Assuming again a collapse length l of 1000 m, comparable to the elastic models, we obtain a geodetic moment of $Mw = 4.3$ (eq. 2).

However, the elasto-plastic model is symmetrical and thus cannot explain the observed asymmetry in the deformation pattern. While the analytical models for the elliptical cavity and the normal fault employ somewhat different rheological assumptions, superimposing the predicted surface deformation pattern (Fig. 3g) provides the best approximation to the observed total subsidence, with an rms misfit of 1.0 cm (Fig. 3h). In this best-fit model the moments from faulting and collapse agree with the seismological data. Solutions with lower contribution from faulting also provide acceptable fits (Table 1).

4 DISCUSSION AND CONCLUSIONS

The deformation pattern associated with the Crandall Canyon mine collapse has generated questions regarding the interaction of mine collapse with pre-existing geological structures—for example did the collapse trigger slip on steeply dipping faults above the cavity? Seismological data suggest that the major source mechanism was implosive (Ford *et al.* 2008; Pechmann *et al.* 2008). Our geodetic deformation models are consistent with the seismological results in the sense that we also require a compound source. However, the models for elastic media require a somewhat larger contribution from normal faulting to fit the data. A hybrid model that includes normal faulting combined with elasto-plastic collapse of an elliptical cavity provides the best fit to the geodetic data and agrees well with the seismological data. The elasto-plastic cavity collapse forms a narrow subsidence wedge (Fig. 7), reducing the amount of fault slip required to fit the data. The asymmetry of the subsidence pattern cannot be modelled with a symmetric collapse, regardless

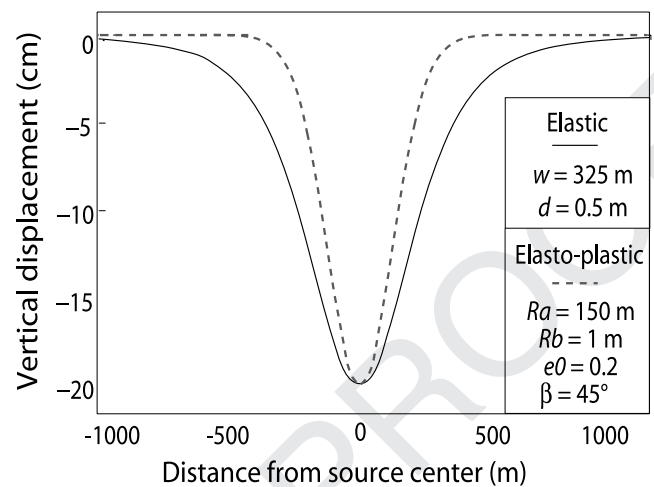


Figure 7. Comparison of width of subsidence trough from elastic collapse model and elasto-plastic collapse model. The source depth (600 m) and horizontal extent of the source are the same in both models. The remaining model parameters are chosen with similar values to cause the same subsidence amplitude. It can be seen that the wedge boundaries in the elasto-plastic model limit the lateral extent of the subsidence trough, causing higher deformation gradients.

of the medium and some normal faulting is required. The amount of normal faulting may be overestimated as we neglect more complicated processes, such as non-uniform cavity closure (Dreger *et al.* 2008) and the effect of topography. However, it was shown that these processes cannot entirely explain the narrow subsidence trough, in particular not in the northeast section of the subsided area (Figs 5a and b). Thus, we conclude that faulting or elasto-plastic material behaviour is still necessary to explain the observations.

Elasto-plastic models are likely to be useful for shallow deformation where unconsolidated material or heavily fractured materials are common, for example, mining areas. Neglecting the elasto-plastic behaviour could bias some parameter estimates.

ACKNOWLEDGMENTS

We thank the reviewers, Douglas Dreger and Ze'ev Reches for helpful advice in improving this manuscript. We also thank Francesca Cigna for helping with the displacement profile calculation. JB was supported by a Rosenstiel Fellowship from the University of Miami and ESA's Changing Earth Science Network. ALOS data was provided by the Alaska Satellite Facility, copyright Jaxa.

REFERENCES

- Buergmann, R., Rosen, P.A. & Fielding, E.J., 2000. Synthetic Aperture Radar Interferometry to measure Earth's surface topography and its deformation, *Annu. Rev. Earth and Planet. Sci.*, **28**, 169–209, doi:10.1146/annurev.earth.28.1.169.
- Carne, C., Massonnet, D. & King, C., 1996. Two examples of the application of SAR interferometry to sites of small extent, *Geophys. Res. Lett.*, **23**, 3579–3582, doi:10.1029/96GL03042.
- Cayol, V. & Cornet, F.H., 1998. Effects of topography on the interpretation of the deformation field of prominent volcanoes—Application to Etna, *Geophys. Res. Lett.*, **25**(11), 1979–1982, doi:10.1029/98GL51512.
- Dreger, D.S., Ford, S.R. & Walter, W.R., 2008. Source analysis of the Crandall Canyon, Utah, Mine collapse, *Science*, **321**, 217, doi:10.1126/science.1157392.

- Ford, S.R., Dreger, D.S. & Walter, W.R., 2008. Source characterization of the August 6, 2007. Crandall Canyon Mine seismic event in central Utah, *Seism. Res. Lett.*, **79**(5), 637–644, doi:10.1785/gssrl.79.5.637.
- Gates, R.A., Gauna, M., Morley, T.A., O'Donnell Jr., J.R., Smith, G.E., Watkins, T.R., Weaver, C.A. & Zelanko, J.C., 2007. Underground Coal Mine, Fatal Underground Coal Burst Accidents August 6 and 16, 2007. United States Department of Labor, Mine Safety and Health Administration, Report of Investigation, CAI-2007–25-27, 19–24.
- Ge, L., Chang, H.C. & Rizos, C., 2007. Mine subsidence monitoring using multi-source satellite SAR images, *J. Photogramm. Eng. Remote Sens.*, **73**(3), 259–266.
- Massonnet, D. & Feigl, K.L., 1998. Radar Interferometry and its application to changes in the Earth's surface, *Rev. Geophys.*, **36**(4), 441–500, doi:10.1029/97RG03139.
- McGarr, A., Spottiswood, S.M. & Gay, N.C., 1975. Relationship of mine tremors to induced stresses and to rock properties in the focal region, *Bull. Seismol. Soc. Am.*, **65**, 981–993.
- Loganathan, N. & Poulos, H.G., 1998. Analytical prediction for tunnelling-induced ground movements in clays, *J. Geotech. Geoenviron. Eng. ASCE*, **124**(9), 846–856, doi:10.1061/(ASCE)1090-0241(1998)124:9(846).
- Lu, Z., submitted. Study of the 6 August 2007 Crandall Canyon mine (Utah, USA) collapse using ALOS PALSAR InSAR.
- Ng, A. H-M., Chang, H-C., Ge, L., Rizos, C. & Omura, M., 2009. Assessment of radar interferometry performance for ground subsidence monitoring due to underground mining, *Earth Planets Space*, **61**, 733–745.
- Okada, Y., 1985. Surface deformation due to shear and tensile faults in a half-space, *Bull. Seismol. Soc. Am.*, **75**, 1135–1154.
- Pechmann, J., Arabasz, W., Pankow, K., Burlacu, R. & McCarter, M., 2008. Seismological Report on the 6 August 2007 Crandall Canyon Mine Collapse in Utah, *Seism. Res. Lett.*, **79**(5), 620–636, doi:10.1785/gssrl.79.5.637.
- Williams, C.A. & Wadge, G., 2000. An accurate and efficient method for including the effects of topography in three-dimensional elastic models of ground deformation with applications to radar interferometry, *J. geophys. Res.*, **105**(B4), 8103–8120, doi:10.1029/1999JB900307.

Q5

UNCORRECTED

Queries

Journal: GJI

Paper: gji_4803

Dear Author

During the copy-editing of your paper, the following queries arose. Please respond to these by marking up your proofs with the necessary changes/additions. Please write your answers on the query sheet if there is insufficient space on the page proofs. Please write clearly and follow the conventions shown on the corrections sheet. If returning the proof by fax do not write too close to the paper's edge. Please remember that illegible mark-ups may delay publication.

Query Reference	Query	Remarks
Q1	Author: Please check and confirm that you are happy with the section (shown on the right-hand side of the title page) to which this paper has been assigned: a list of all the sections can be found in the Author Guidelines (http://www.wiley.com/bw/submit.asp?ref=0956-540X&site=1).	
Q2	Author: Please provide the expanded form of SRTM DEM.	
Q3	Author: Please supply a short title of up to 45 characters that will be used as the running head.	
Q4	Author: Please check the reference Hanks & Kanamori (1979) is not present in the reference list, provide full publication details.	
Q5	Author: Please update the reference Lu (submitted). Also this reference is not cited in the text.	

Key words

Authors are requested to choose key words from the list below to describe their work. The key words will be printed underneath the summary and are useful for readers and researchers. Key words should be separated by a semi-colon and listed in the order that they appear in this list. An article should contain no more than six key words.

GEOPHYSICAL METHODS

Time series analysis
Image processing
Neural networks, fuzzy logic
Numerical solutions
Fourier analysis
Wavelet transform
Instability analysis
Inverse theory
Numerical approximations and analysis
Persistence, memory, correlations, clustering
Probabilistic forecasting
Spatial analysis
Downhole methods
Tomography
Interferometry
Thermobarometry
Fractals and multifractals
Non-linear differential equations
Probability distributions
Self-organization

GEODESY and GRAVITY

Satellite geodesy
Reference systems
Sea level change
Space geodetic surveys
Seismic cycle
Transient deformation
Gravity anomalies and Earth structure
Geopotential theory
Time variable gravity
Earth rotation variations
Global change from geodesy
Lunar and planetary geodesy and gravity
Radar interferometry
Plate motions
Tides and planetary waves
Acoustic-gravity waves

GEOMAGNETISM and ELECTROMAGNETISM

Electrical properties
Electromagnetic theory
Magnetotelluric
Non-linear electromagnetics
Archaeomagnetism
Biogenic magnetic minerals
Dynamo: theories and simulations
Environmental magnetism
Geomagnetic excursions
Geomagnetic induction
Ground penetrating radar
Magnetic anomalies: modelling and interpretation
Magnetic and electrical properties
Magnetic fabrics and anisotropy
Magnetic field
Magnetic mineralogy and petrology
Magnetostratigraphy

Palaeointensity
Palaeomagnetic secular variation
Palaeomagnetism applied to tectonics
Palaeomagnetism applied to geologic processes
Rapid time variations
Remagnetization
Reversals: process, time scale, magnetostratigraphy
Rock and mineral magnetism
Satellite magnetics
Marine magnetics and palaeomagnetics
Marine electromagnetics

GENERAL SUBJECTS

Geomorphology
Geomechanics
Glaciology
Hydrogeophysics
Ionosphere/atmosphere interactions
Ionosphere/magnetosphere interactions
Gas and hydrate systems
Ocean drilling
Instrumental noise
Hydrology
Ultra-high pressure metamorphism
Ultra-high temperature metamorphism
Tsunamis
Thermochronology
Heat flow
Hydrothermal systems
Mantle processes
Core, outer core and inner core

COMPOSITION and PHYSICAL PROPERTIES

Microstructures
Permeability and porosity
Plasticity, diffusion, and creep
Composition of the core
Composition of the continental crust
Composition of the oceanic crust
Composition of the mantle
Composition of the planets
Creep and deformation
Defects
Elasticity and anelasticity
Equations of state
High-pressure behaviour
Fracture and flow
Friction
Fault zone rheology
Phase transitions

SEISMOLOGY

Controlled source seismology
Earthquake dynamics
Earthquake ground motions
Earthquake source observations

Broad-band seismometers
Seismic monitoring and test-ban treaty verification
Palaeoseismology
Earthquake interaction, forecasting, and prediction
Seismicity and tectonics
Body waves
Surface waves and free oscillations
Interface waves
Guided waves
Coda waves
Seismic anisotropy
Seismic attenuation
Site effects
Seismic tomography
Volcano seismology
Computational seismology
Theoretical seismology
Statistical seismology
Wave scattering and diffraction
Wave propagation
Acoustic properties
Early warning
Rheology and friction of fault zones

TECTONOPHYSICS

Planetary tectonics
Mid-ocean ridge processes
Transform faults
Subduction zone processes
Intra-plate processes
Volcanic arc processes
Back-arc basin processes
Cratons
Continental margins: convergent
Continental margins: divergent
Continental margins: transform
Continental neotectonics
Continental tectonics: compressional
Continental tectonics: extensional
Continental tectonics: strike-slip and transform
Sedimentary basin processes
Oceanic hotspots and intraplate volcanism
Oceanic plateaus and microcontinents
Oceanic transform and fracture zone processes
Submarine landslides
Submarine tectonics and volcanism
Tectonics and landscape evolution
Tectonics and climatic interactions
Dynamics and mechanics of faulting
Dynamics of lithosphere and mantle
Dynamics: convection currents, and mantle plumes
Dynamics: gravity and tectonics
Dynamics: seismotectonics
Heat generation and transport

Impact phenomena
 Hotspots
 Large igneous provinces
 Lithospheric flexure
 Obduction tectonics
 Neotectonics
 Diapir and diapirism
 Folds and folding
 Fractures and faults
 Kinematics of crustal and mantle
 deformation
 High strain deformation zones
 Crustal structure
 Mechanics, theory, and modelling
 Rheology: crust and lithosphere
 Rheology: mantle

PLANETS
 Planetary interiors
 Planetary volcanism

VOLCANOLOGY
 Physics of magma and
 magma bodies
 Magma chamber processes
 Magma genesis and partial melting
 Pluton emplacement
 Effusive volcanism
 Mud volcanism
 Subaqueous volcanism
 Explosive volcanism
 Volcaniclastic deposits
 Volcano/climate interactions
 Atmospheric effects (volcano)
 Volcanic gases
 Lava rheology and morphology
 Magma migration and fragmentation
 Eruption mechanisms and
 flow emplacement
 Physics and chemistry of magma
 bodies

Calderas
 Experimental volcanism
 Tephrochronology
 Remote sensing of volcanoes
 Volcano monitoring
 Volcanic hazards and risks

GEOGRAPHIC LOCATION
 Africa
 Antarctica
 Arctic region
 Asia
 Atlantic Ocean
 Australia
 Europe
 Indian Ocean
 New Zealand
 North America
 Pacific Ocean
 South America

MARKED PROOF

Please correct and return this set

Please use the proof correction marks shown below for all alterations and corrections. If you wish to return your proof by fax you should ensure that all amendments are written clearly in dark ink and are made well within the page margins.

<i>Instruction to printer</i>	<i>Textual mark</i>	<i>Marginal mark</i>
Leave unchanged	... under matter to remain	Ⓢ
Insert in text the matter indicated in the margin	λ	New matter followed by λ or λ [Ⓢ]
Delete	/ through single character, rule or underline or ┌───┐ through all characters to be deleted	σ or σ [Ⓢ]
Substitute character or substitute part of one or more word(s)	/ through letter or ┌───┐ through characters	new character / or new characters /
Change to italics	— under matter to be changed	⎵
Change to capitals	≡≡ under matter to be changed	≡≡
Change to small capitals	== under matter to be changed	==
Change to bold type	~ under matter to be changed	~
Change to bold italic	≈ under matter to be changed	≈
Change to lower case	Encircle matter to be changed	⊖
Change italic to upright type	(As above)	⊕
Change bold to non-bold type	(As above)	⊖
Insert 'superior' character	/ through character or λ where required	γ or λ under character e.g. γ̇ or λ̇
Insert 'inferior' character	(As above)	λ over character e.g. λ̇
Insert full stop	(As above)	⊙
Insert comma	(As above)	,
Insert single quotation marks	(As above)	γ̇ or λ̇ and/or γ̇ or λ̇
Insert double quotation marks	(As above)	γ̇ or λ̇ and/or γ̇ or λ̇
Insert hyphen	(As above)	⎵
Start new paragraph	┌	┌
No new paragraph	~	~
Transpose	┌┐	┌┐
Close up	linking ○ characters	○
Insert or substitute space between characters or words	/ through character or λ where required	γ
Reduce space between characters or words		↑